A Hybrid Surgical Robotic System for High-Dexterity Vitreoretinal Surgery

Haochen Wei[1*], Teng Long[2*], Yub Heo[3*], Botao Zhao[3], Mojtaba Esfandiari[3], Chongyang She[2]
Adnan Munawar[2], Peter Gehlbach[4], Peter Kazanzides[1], and Iulian Iordachita[3]

Abstract— This work develops a hybrid surgical robotic system with seven degrees of freedom (7-DoF), including a 5-DoF base robot (BR), integrated with a 2-DoF snake robot (SR) at the distal end, aiming to perform epiretinal membrane (ERM) peeling, safely and efficiently, with optimum approach angle. A model predictive control (MPC) algorithm is designed to satisfy a remote center of motion (RCM) constraint for the BR at the sclerotomy port, while controlling the SR at the distal end. The accuracy of the robot's kinematics and MPC controller for the RCM constraint and the tool's approach angle to the retina surface is measured and analyzed in an artificial eye phantom. Moreover, the performance of the hybrid robotic platform is evaluated in a pilot study with five users, in a teleoperation experiment targeting a random order of target points, with and without the use of the SR. Experimental results demonstrate significant improvement in users' performance in terms of task completion time, counts of clutch activations, and success rate, while using the hybrid system (BR $\&$ SR) compared to the case using only the BR.
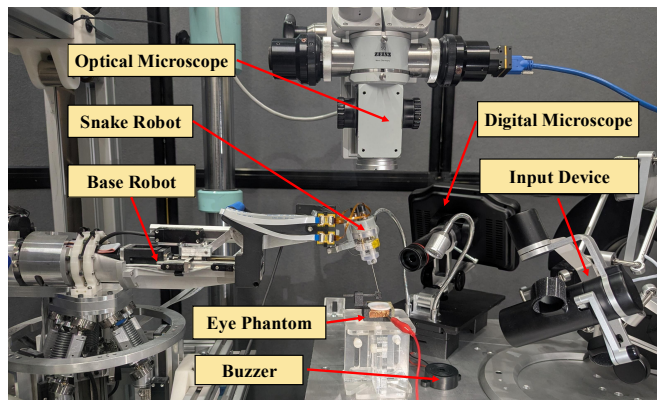
Fig. 1: System overview, with the combined BR and SR, input device for teleoperation, optical and digital microscopes for visual feedback, eye phantom, and buzzer.

I. INTRODUCTION

Vitreoretinal surgery is a microsurgical technique used to treat diseases of the retina and the posterior segment of the eye. Due to the extremely small intraocular structures and the fragility and non-regenerative nature of the retina, it is considered one of the most technically demanding procedures in ophthalmology [1]. Among these procedures, surgeons must peel membranes from the retina, which is currently the most commonly performed vitreoretinal surgery in the United States. During epiretinal membrane (ERM) peeling, surgeons carefully grasp and peel away a thin (on average 61±28 μm [2]), fibrous membrane that forms on the surface of the retina after performing a pars-plana vitrectomy to create access. This surgery aims to restore the retinal architecture and improve visual function.

The procedure presents significant challenges. Depending on patient-specific conditions, the reported complication rates range from 2% to 30%, with mechanical retinal injury being the most critical concern. Such injuries often result from excessive peeling forces, which are strongly influenced by both the speed and angle of membrane detachment [3]. These difficulties highlight the intrinsic limitations of human manual dexterity at the microscale. Consequently, the development and deployment of robotic systems to assist or replace manual operation has emerged as a natural progression [4], offering the potential for enhanced precision, consistency, and safety in vitreoretinal surgery.

To date, robotic systems outside ophthalmology—such as the da Vinci surgical platform (Intuitive Surgical Inc., Sunnyvale, CA, USA)—provide up to seven degrees of freedom at the instrument tip, enabling wrist-like articulation that significantly enhances operative flexibility [5]. In contrast, the development of comparable ophthalmic platforms remains at a relatively early stage. Existing ophthalmic robotic systems, such as SMOS [6], Preceyes [7], and RAMS [8] have primarily focused on filtering out physiological tremor, enhancing control precision, and maintaining the remote center of motion (RCM). While these systems achieve stable manipulation, their distal flexibility remains limited, and they do not yet provide the ability to freely control peeling direction in ERM surgery. This gap motivates the present work. Continuum robots have the potential to provide the necessary dexterity to perform ERM peeling [9]. Integrating continuum robots with existing base robotic platforms can provide an optimal approach angle to perform ERM peeling safely and efficiently. However, modeling of continuum robots could be difficult due to mechanical nonlinearities such as hysteresis and lack of embedded sensing modules, making precise control of these robots a challenging problem [10].

*These authors contributed equally to this work.

[1]Department of Computer Science, Johns Hopkins University, Baltimore, MD, 21218, USA, {hwei15,pkaz}@jhu.edu

[2]Laboratory for Computational Sensing and Robotics, Johns Hopkins University, Baltimore, MD, 21218, USA, {tlong29,cshe1,amunawa2}@jhu.edu

[3]Department of Mechanical Engineering, Johns Hopkins University, Baltimore, MD, 21218, USA, {yheo1,bzhao17,mesfand2,iordachita}@jhu.edu

[4]Wilmer Eye Institute, Johns Hopkins School of Medicine, Baltimore, MD, 21287, USA, pgelbach@jhmi.edu

The main contributions from this paper are as follows:

- We combine a previously developed snake-like distal mechanism [11] with a base robotic platform [12] to construct a fully integrated ophthalmic robotic system shown in Fig. 1
- We design a novel control method tailored for ERM peeling by coordinating the concurrent operation of the two robots with a single 6-DoF input device.

To validate this, several experiments are conducted, including a pilot study to evaluate the feasibility and performance of the combined system.

II. MATERIALS AND METHODS

A. System

As illustrated in Fig. 2, the proposed medical robotic system is composed of two major components: a base robot (BR) and a snake robot (SR). The BR, developed in prior work [12], provides core functionalities commonly found in existing teleoperated robotic platforms, including tremor attenuation, a remote center of motion (RCM) constraint, and stable end-effector positioning. The SR, also developed in previous work [11], is serially mounted on the end effector of the BR. It is independently actuated and controlled to provide enhanced dexterity beyond traditional straight-shaft instruments, thereby enabling complex intraoperative maneuvers in confined anatomical spaces.

Both BR and SR are independently connected to a main computer. The BR is driven by a Galil DMC controller (Galil Motion, Rocklin, CA) communicating via Ethernet, while the SR is driven by a Maxon EPOS2 controller (Maxon Group, Sachseln, Switzerland) communicating via USB. To ensure low-latency and reliable communication, we employ the *anonymous* software framework [13] as the middleware layer for inter-module messaging and synchronization. For
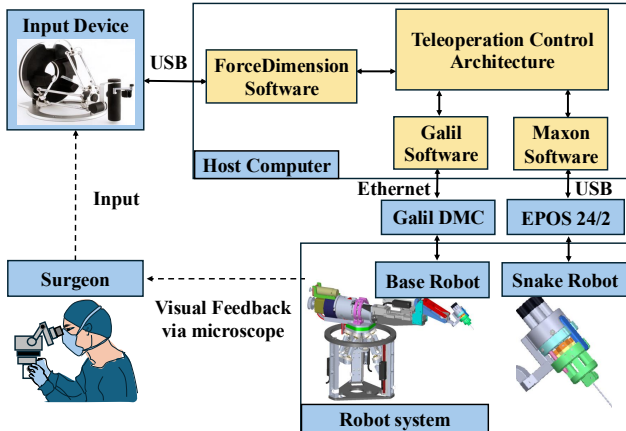

Fig. 2: System architecture, including the surgeon input through the Omega 7 input device, mid-level controller with software modules, and the two independent robot parts, SR and BR. Visual feedback is provided via the microscopes to close the control loop. Specific component names are redacted for double blind review.

operator input, the system utilizes a haptic device (Omega.7, Force Dimension, Nyon, Switzerland), which is connected to the main computer via USB and integrated into the control pipeline through the aforementioned framework. The haptic device was only used for motion input. This modular system architecture allows for real-time coordination of BR and SR, while maintaining flexibility in mid-level controller design.
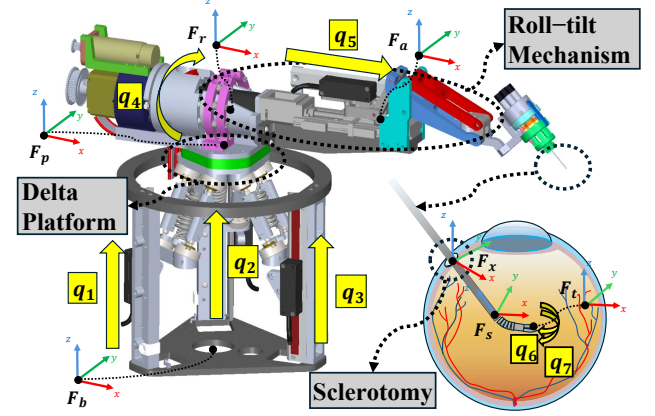
B. Kinematics

Fig. 3: Kinematic diagram of combined system, showing the base frame F_b, platform frame F_p, roll frame F_r, tilt frame F_a, RCM frame F_x, shaft frame F_s and tip frame F_t. The kinematics between frame F_b, F_p, F_r, F_t are described in previous works [14], [15]. The kinematics between frame F_s and F_t is described in Eq. 6

1) Base Robot: The BR is a 5-DOF robotic system, comprising two serially connected subsystems: a parallel delta mechanism for tool positioning and a roll-tilt four-bar mechanism for tool orientation. The kinematic modeling and reference frames of the delta and roll-tilt mechanisms are detailed in [14], [15]. The overall Jacobian of the BR can be expressed in block form as:

$$J_{BR} = \left[\begin{array}{c|c} J_D \\ \mathbf{0}_{3\times3} \end{array} \middle| J_{RT} \right] \quad (1)$$

where $J_D \in \mathbb{R}^{3\times3}$ is the Jacobian of the delta positioning platform, controlled by joints q_1, q_2, and q_3, as shown in Fig. 3. $J_{RT} \in \mathbb{R}^{6\times2}$ is the Jacobian of the roll-tilt mechanism, controlled by joints q_4 and q_5. The end-effector velocity in the base frame can then be expressed as:

$$V = J_{BR}\,\dot{q} \quad (2)$$

where V is the spatial velocity of the end effector and $\dot{q}$ is the vector of joint velocities, given by:

$$V = [\dot{x}, \dot{y}, \dot{z}, \dot{\theta}_x, \dot{\theta}_y, \dot{\theta}_z]^T$$
$$\dot{q} = [\dot{q}_1, \dot{q}_2, \dot{q}_3, \dot{q}_4, \dot{q}_5]^T \quad (3)$$

2) Snake Robot: The SR is a 2-DOF cable-driven micro-continuum robot consisting of 13 disc-like elements that allow for dexterous motion. As detailed in previous works [11], [16], the elements are of thickness $h_e = 0.15\,\text{mm}$, diameter $D = 0.9\,\text{mm}$, and consist of cylindrical surfaces $r = 0.8\,\text{mm}$ on each side that are orthogonal to each other. Each element makes contact with the cylindrical surface of the subsequent element. To actuate the SR, an off-axis drive mechanism is used to push/pull two cables that are routed through an entrance point and each segment. Rotation of the drive pulley causes cable displacement due to an intentional displacement between the rotational axis of the pulley and the central axis of the shaft. The cable displacement then bends the SR to its desired bending angle (see Fig. 4(a)). A simple mapping function is used to map the cable displacement to the bending angle.

In this model, the discs of each element rotate by rolling on their respective surfaces (see Fig. 4). As such, the transformation from one element to the next can be derived by forming disc joints where the origin of the cylindrical surfaces are $2r$ apart (Fig. 4(d)). Each disc joint is oriented $90°$ along the shaft axis from the previous pair. The two sets of joints allow bending along the yaw and pitch, and it is assumed that every pair in the set has identical bending angle (Fig. 4(e)&(f)). Given 12 disc joints and the desired bending angle, the bending angle for each pair can be determined.

$$\phi_{pair} = \frac{\phi_{des}}{6}, \quad \psi_{pair} = \frac{\psi_{des}}{6} \tag{4}$$

In this model, bending in the pitch and yaw directions is assumed to correspond to pure rotations about the local x-axis and y-axis, respectively. Under this assumption, we can derive the transformation matrix between each disc joint. Eq. 5, where $\theta = \phi_{pair}$, shows the transformation matrix for the pitch rotation. Similarly, the transformation matrix can be derived for the yaw rotation, ψ_{pair}.

$$T^{\text{disc}} = \begin{bmatrix} 1 & 0 & 0 & 0 \\ 0 & \cos(\theta) & -\sin(\theta) & r\left(\sin(\theta) - 2\sin(\frac{\theta}{2})\right) \\ 0 & \sin(\theta) & \cos(\theta) & h_e + 2r\left(\cos(\frac{\theta}{2}) - \cos^2(\frac{\theta}{2})\right) \\ 0 & 0 & 0 & 1 \end{bmatrix} \tag{5}$$

With 12 disc joints in the continuum robot, the transformation of the gripper with respect to its base, T_t^s, can be derived, given the desired pitch, yaw, and the transformation between the gripper element base F_g and its tip F_t, $T_{gripper}$:

$$T_t^s = \left(T_{\text{pitch}}^{\text{disc}} \cdot T_{\text{yaw}}^{\text{disc}}\right)^6 \cdot T_{gripper} \tag{6}$$

The derivative of Eq. 5, with respect to ϕ_{pair} is then used with Eqns. 4 & 6 to obtain the Jacobian of the micro-continuum robot (see Eq. 7).

$$T'_{pitch} = \frac{\partial T_{\text{pitch}}^{\text{disc}}}{\partial \phi_{pair}}, \quad T'_{yaw} = \frac{\partial T_{\text{yaw}}^{\text{disc}}}{\partial \psi_{pair}} \tag{7}$$

The overall Jacobian, $J_{SR} \in \mathbb{R}^{6\times 2}$ can be expressed as

$$J_{SR} = \begin{bmatrix} \frac{\partial T_t^s}{\partial \phi_{des}} & \frac{\partial T_t^s}{\partial \psi_{des}} \end{bmatrix} \tag{8}$$
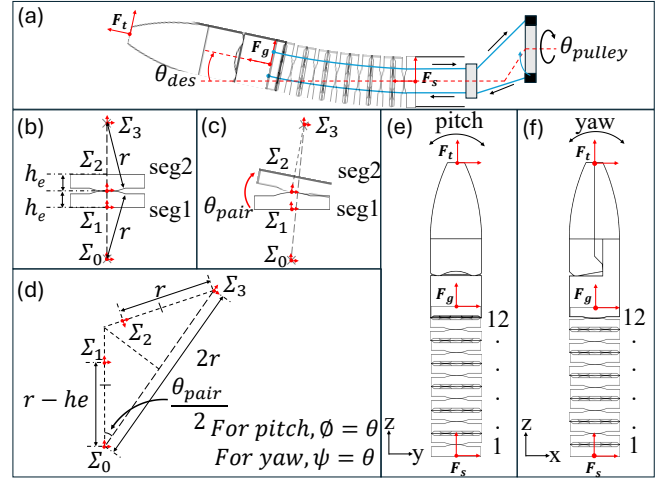

Fig. 4: Kinematic analysis of the SR's elements: (a) drive mechanism (b) initial state; (c) bending state; (d) magnified view of bending state; (e) x-z cross sectional-view; (f) y-z cross sectional-view

For the pitch input,

$$\begin{aligned} \frac{\partial T_{SR}}{\partial \phi_{des}} = \frac{1}{6}\Big[&\left(T'_{pitch} \cdot T_{\text{yaw}}^{\text{disc}}\right) \cdot \left(T_{\text{pitch}}^{\text{disc}} \cdot T_{\text{yaw}}^{\text{disc}}\right)^5 \\ &+ \left(T_{\text{pitch}}^{\text{disc}} \cdot T_{\text{yaw}}^{\text{disc}}\right)\left(T'_{pitch} \cdot T_{\text{yaw}}^{\text{disc}}\right)\left(T_{\text{pitch}}^{\text{disc}} \cdot T_{\text{yaw}}^{\text{disc}}\right)^4 \\ &+ \dots \\ &+ \left(T_{\text{pitch}}^{\text{disc}} \cdot T_{\text{yaw}}^{\text{disc}}\right)^5 \left(T'_{pitch} \cdot T_{\text{yaw}}^{\text{disc}}\right)\Big] \cdot T_{gripper} \end{aligned} \tag{9}$$

The Jacobian for yaw input can be similarly derived with the derivative of Eq. 5, with respect to ψ_{pair}.

C. Model Predictive Controller for RCM Constraint

During vitreoretinal surgery, the tool has to be inserted through the sclerotomy (See Fig. 3). Therefore, the robot's motion must be constrained to an RCM [17] (Frame F_x is established at the RCM shown in Fig. 3) in line with the sclerotomy, together with additional velocity constraints in both the joint space and the tool Cartesian space. MPC [18], [19] is adopted as the main control strategy, where the system state at time t is defined as the tool tip pose,

$$\chi_t = \{x, y, z, roll, pitch, 0\}, \tag{10}$$

and the system input at time t is defined as

$$u_t = \{\dot{q}_1, \dot{q}_2, \dot{q}_3, \dot{q}_4, \dot{q}_5\}, \tag{11}$$

where $\dot{q}_i$ denotes the i-th joint velocity.

The cost function for the MPC formulation is defined as

$$\begin{aligned} J = \sum_{t=0}^{n-1} &\left[(\chi_t - \chi_{\text{des}})^T Q(\chi_t - \chi_{\text{des}}) + u_t^T R u_t + d_t^T M d_t\right] \\ &+ \chi_n^T Q_f \chi_n. \end{aligned} \tag{12}$$

s.t.

$$Q \succeq 0, \ R \succ 0, \ M \succeq 0, \ Q_f \succeq 0,$$
$$\chi_{t+1} = \chi_t + J_{BR}(q_t)u_t \, dt,$$
$$q_{t+1} = q_t + u_t \, dt,$$
$$d_t = \|(p_{\text{RCM}} - p_0) \times \hat{s}_t\|,$$
$$\dot{q}_{\min} \leq u_t \leq \dot{q}_{\max},$$
$$\dot{\chi}_{\min} \leq J_{BR}(q_t)u_t \leq \dot{\chi}_{\max}.$$

where the prediction horizon n in our model is 10. χ_{des} denotes the desired tip position provided by the translation signal of the input device. $J_{BR}(q_t) \in \mathbb{R}^{6\times 5}$ denotes the Jacobian matrix of the BR in Eq. 1 evaluated at the joint configuration q_t. d_t is the distance between the tool shaft and the RCM point, $p_{\text{RCM}} \in \mathbb{R}^3$ is the position vector of the RCM, p_0 corresponds to the tool tip position, and $\hat{s}_t$ is the unit direction vector of the shaft.

D. Teleoperation Control Strategy for Combined Robot

In the combined robotic teleoperation system, we employ a dual-loop control architecture to accommodate the heterogeneous sampling rates and dynamics of the two robots. Fig. 5 represents the overall control diagram. The operator operates the input device, where the desired translation signals x_{des}, y_{des} and z_{des} are used to drive the BR, while the desired rotation signals $roll_{des}$ and $pitch_{des}$ set the orientation of the SR.

1) Base Robot Control Loop: The desired position signal is fed to the MPC-based optimal controller in Eq. 12, which outputs the joint-velocity command $\dot{q}_{des}^{BR} \in \mathbb{R}^5$ for all five joints of the BR. A motion limit block guarantees safe execution of the commanded motion. Its output $\dot{q}_{des}^{BR'}$ is defined as

$$\dot{q}_{des}^{BR'} = \begin{cases} 0, & \alpha = 0 \\ E^T \dot{q}_{des}^{BR}, & otherwise \end{cases} \tag{13}$$

where α represents a binary activation signal from the clutch pedal. The function $E \in \mathbb{R}^5$ constrains the motion along prescribed directions influenced by the translational inputs, x_{des}, y_{des}, z_{des} from the input device, and the current Cartesian velocity $\dot{\chi}_{real}^{BR} \in \mathbb{R}^6$ of the BR's end-effector in frame F_s (shown in Fig. 3). Eventually, the final desired joint velocity $\dot{q}_{real}^{BR'} \in \mathbb{R}^5$ is transmitted to the low-level Galil controller, which generates the control commands to achieve the target velocities for all five joints of the BR. Other signals include $\dot{q}_{real}^{BR} \in \mathbb{R}^5$,(actual joint velocity of BR), which is used to update the Jacobian J_{BR} in Eq. 1 and then generates the Cartesian velocity $\dot{\chi}_{real}^{BR}$ of the end effector.

2) Snake Robot Control Loop: To control the SR, two rotational signals, $roll_{des}$ and $pitch_{des}$ from the input device handle are used to form the desired tip angle. A PD controller is used to give the velocity commands $\dot{q}_{des}^{SR} \in \mathbb{R}^2$ to two Maxon motors, which drive the cable mechanism that actuates the SR. Based on feedback from the motor encoders,

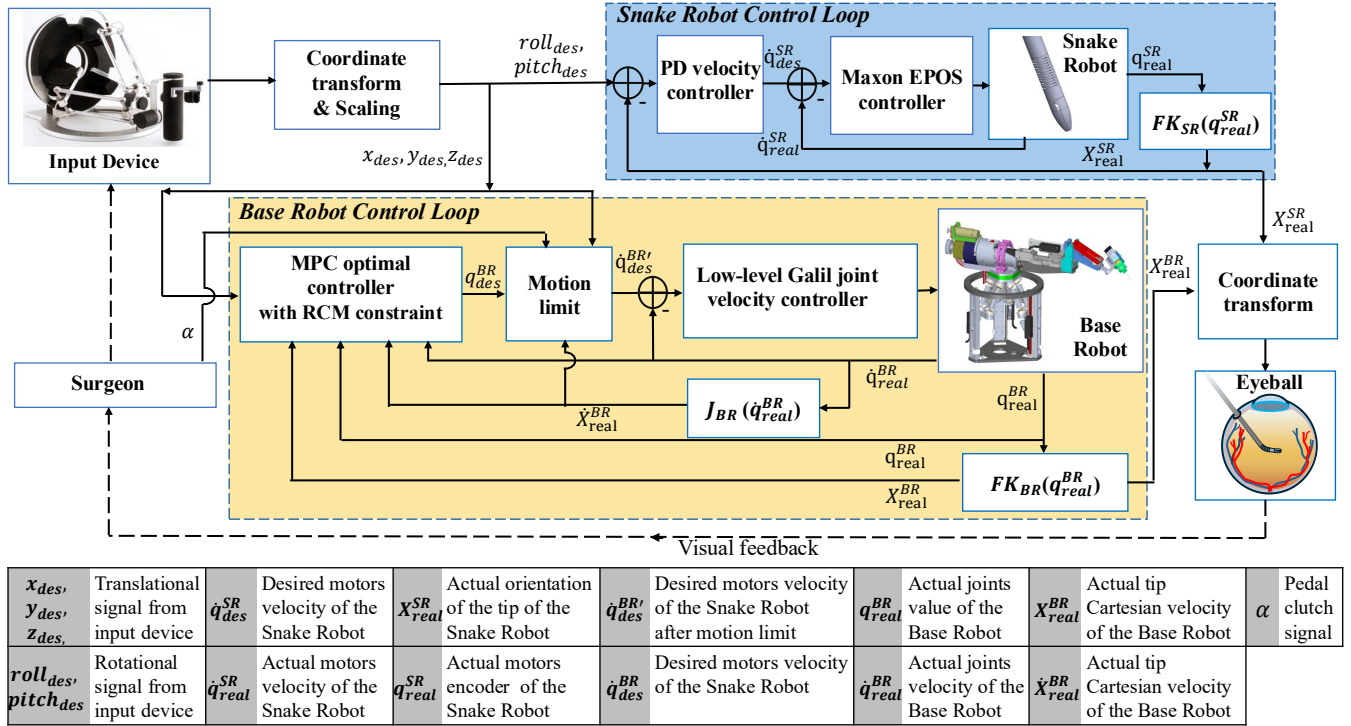| x_{des}, y_{des}, z_{des}	Translational signal from input device	$\dot{q}_{des}^{SR}$	Desired motors velocity of the Snake Robot	X_{real}^{SR}	Actual orientation of the tip of the Snake Robot	$\dot{q}_{des}^{BR'}$	Desired motors velocity of the Snake Robot after motion limit	q_{real}^{BR}	Actual joints value of the Base Robot	X_{real}^{BR},	Actual tip Cartesian velocity of the Base Robot	α	Pedal clutch signal
$roll_{des}$, $pitch_{des}$	Rotational signal from input device	$\dot{q}_{real}^{SR}$	Actual motors velocity of the Snake Robot	q_{real}^{SR}	Actual motors encoder of the Snake Robot	$\dot{q}_{des}^{BR}$	Desired motors velocity of the Snake Robot	$\dot{q}_{real}^{BR}$	Actual joints velocity of the Base Robot	$\dot{X}_{real}^{BR}$	Actual tip Cartesian velocity of the Base Robot		

Fig. 5: Block diagram of the teleoperation control architecture. The outer loop implements high-level control with surgeon commands and visual feedback; the middle loop runs the core teleoperation algorithm, that combines the BR control loop (yellow area) and SR control loop (blue area); the inner loop drives the Galil controller to move the BR's motors and the Maxon motors move the SR's motors.
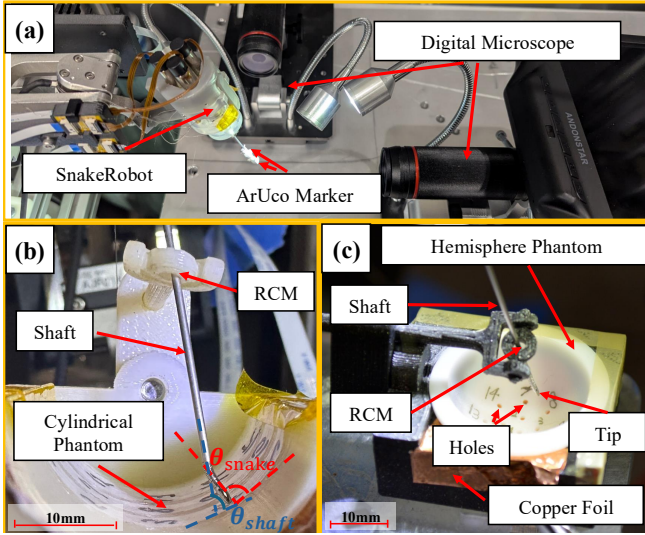
Fig. 6: (a) Insertion accuracy setup for y-z axis viewpoint, including 3 mm ArUco marker and digital microscope; (b) Dual-robot teleoperation setup, including RCM constraint and cylindrical phantom; (c) Pilot user study setup; including hemisphere phantom with insertion holes, RCM constraint and copper foil for contact detection.

the real snake tip orientation is estimated with the forward kinematics in Eq. 6 of the SR, and the calculated result is $\dot{\chi}_{real}^{SR}$.

In the high-level control loop, the combined effect of the two robot's individual control loops is ultimately manifested in the intraocular motion of the SR. Under the operating microscope, the surgeon manipulates the input device handle and the foot pedal to achieve precise control.

III. EXPERIMENTS

Three different experiments are conducted to evaluate the overall performance of the proposed medical robotic system. The experiments and their associated goals are:

1) Insertion accuracy: To evaluate the positional accuracy of the proposed control method for the robotic system.
2) Dual-robot teleoperation study: To evaluate concurrent independent teleoperation of both robots with a single input device.
3) Multi-user pilot study: To evaluate the usability of the proposed intraocular surgical robot and teleoperation control strategy.

A. Insertion Accuracy

1) Experimental Setup: The experiment setup is presented in Fig. 6(a), and consists of the medical robotic system, 3 mm ArUco markers, and a digital microscope (AD407, Andonstar, China). Vision-based tracking of the ArUco markers is used to assess insertion accuracy. The ArUco markers are rigidly attached to the robot's end-effector, and the digital microscope is calibrated using a standard pinhole model. Based on a first-order linear approximation, the physical

error σ is given by

$$\sigma \approx \frac{Z}{f}\,\sigma_{pix} \qquad (14)$$

where Z the distance between the camera and the object, f the focal length, and σ_{pix} is the pixel wise detection error. To account for calibration error, the root-sum-square of reprojection error from calibration and pixel wise detection error is used as the total effective error. Two orthogonal viewpoints are used to ensure that measurements capture potential errors along perpendicular directions of motion. Since the BR is actuated by a delta stage mechanism, only translational motions are considered for this evaluation.

The root mean square (RMS) reprojection error from calibration is evaluated to be 1.20 px, with a focal length of 23970 px and 24406 px in the x and y directions of the image, respectively. The physical distance between the marker and the camera is estimated as around 200 mm, based on marker detection. While the depth error is in the millimeter scale, it has a very low effect on the overall final accuracy calculation. The actual pixel wise physical resolution is estimated to be approximately 10 $\mu m/px$.

2) Experimental Procedure: The experimental procedure begins with the robot in its home position. The robot is then commanded to insert the instrument tip by 1 mm along the direction of the instrument shaft. The displacement of the ArUco markers is subsequently measured using a digital microscope. Because ArUco markers cannot directly detect off-axis movement, we averaged the images acquired before and after the movement and manually counted the pixels to estimate the off-axis displacement. The experiment is conducted at three different target speeds: $1mm/s$, $0.5mm/s$, and $0.1mm/s$. Each speed is repeated for 4 times, shown result is the average movement.

B. Dual-robot Teleoperation Study

1) Experimental Setup: The experiment setup for the dual-robot teleoperation study is presented in Fig. 6(b), and consists of the medical robotic system, a cylindrical phantom, digital microscope, and an input device. The cylindrical phantom is of human eye diameter ($D = 24$ mm) and has a gimbal joint as the RCM to mimic the sclerotomy. A concurrent teleoperation task is used to assess the teleoperation control strategy. The instrument shaft of the robotic system is placed through the RCM constraint. The digital microscope is placed orthogonal to the phantom such that the angle of the instrument tip and shaft along the inner surface of the phantom can be viewed.

2) Experimental Procedure: The experiment includes a total of 10 trials by a single user. For each trial, the user is asked to teleoperate both robots with the input device handle and sweep the instrument along the cylindrical surface while keeping the approach angle of the tip normal to the surface. 5 equally distributed points along the surface ($-20°$ to $20°$) are used as reference points. The approach angles of the shaft and tip are measured when the tip is in line with each reference point.

C. Pilot User Study

1) Experimental Setup: The experiment setup for the pilot user study is presented in Fig. 6(c). and Fig. 1. It includes similar devices to the previous experimental setup, with changes to the phantom (hemispherical phantom) and microscope (OPMI 1, Carl Zeiss Microscopy, Oberkochen, Germany), and an added buzzer. The hemispherical phantom is of human eye diameter ($D = 24\,$mm) and has an RCM constraint to mimic the sclerotomy. The inner surface of the phantom is lined with copper foil, which is connected to the buzzer. Insertion holes in the phantom allow for insertion detection between the instrument tip and the hole. The optical microscope is used to get an illuminated, top-down view of the hemispherical surface of the phantom and the robot shaft during manipulation.

2) Experimental Procedure: Prior to the study, each user is given 10 minutes to practice with the system. To evaluate the usability of the proposed robotic system, the user is asked to insert the instrument tip into 5 randomly sequenced holes. A total of 5 trials per user is performed, with the hole sequences for each trial kept consistent across all users. The user is also asked to perform the same insertion task with the SR disabled, to mimic a more traditional vitreoretinal surgical robot with a straight tool, as opposed to the snake tool of the proposed robotic system. Users were randomized and counterbalanced to start with either the straight or snake tool. After the study, participants completed a NASA-TLX questionnaire to assess mental workload for both tools. Completion time and number of clutch activations were measured for evaluation as well.

IV. EXPERIMENTAL RESULTS AND ANALYSIS

A. Insertion Accuracy

Table I presents the results of the insertion accuracy experiment. Comparable overshoot across different insertion velocities indicates that overshoot is not strongly correlated to robot speed. This suggests that the error is not primarily due to stopping distance. This experiment demonstrates that the accuracy of our system has not yet met the desired expectations. While the off-axis displacement is smaller compared to the overshoot, it remains non-negligible. However, since no compensation or calibration has been applied beyond the theoretical kinematic model, achieving sub-millimeter accuracy is already an encouraging result. It is intended to perform kinematic calibration to further improve system accuracy.

B. Dual-robot Teleoperation

To evaluate concurrent independent control during teleoperation, we compared the angle of the distal tip and shaft relative to the tangent of the surface during a sweeping task. Fig. 6 shows the definition of the angle of snake θ_{snake} and angle of shaft θ_{shaft}. A consistent θ_{snake} across all reference points, as compared to the θ_{shaft}, would indicate independent teleoperative control of the BR and SR. Fig. 7 illustrates the mean angle across 10 trials of the sweeping task. It is observed that the snake maintains relatively normal

TABLE I: Insertion accuracy at different velocities and measuring positions. Front represents measurement from the front, where camera optical axis is parallel with x-axis of Frame F_s defined in Fig.3. Side represents measurement along the y-axis of the same frame. Off-axis represents misalignment of movement from the desired axis. The average represents the absolute average movement. All units are in μm

Insertion Speed	1000 µm/s	500 µm/s	100 µm/s
Front	1118	1115	1111
Side	1145	1083	1132
Off-axis Front	31	72	51
Off-axis Side	72	67	57
Average	**1132**	**1099**	**1122**

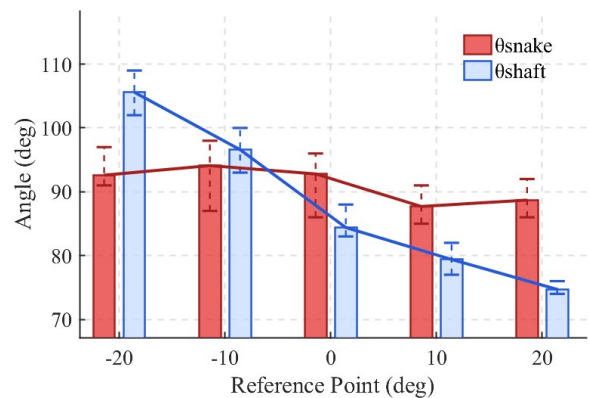Fig. 7: Comparison of approach angles of the snake vs. the shaft across reference points.

orientation (see blue curve in Fig. 7) while the θ_{shaft} decreases (see red curve in Fig. 7) across reference points due to mechanical limitations from the RCM. Of note, due to the nature of teleoperative control, maintaining the distal tip consistently normal to the surface is difficult. However, it still validates the ability of the teleoperative control strategy to provide the user's desired approach angles of the tool during manipulation with a single input device.

One limitation of this study is that the approach angles of the snake do not completely mimic the optimum approach angles during procedures such as ERM peeling (tangential peeling vs snake normal to surface). As future work, guiding the user with optimum approach angles during vitreoretinal surgical tasks through the input device handle will be considered.

C. Pilot User Study

To evaluate targeting performance in our teleoperation framework, we compared the results achieved with the
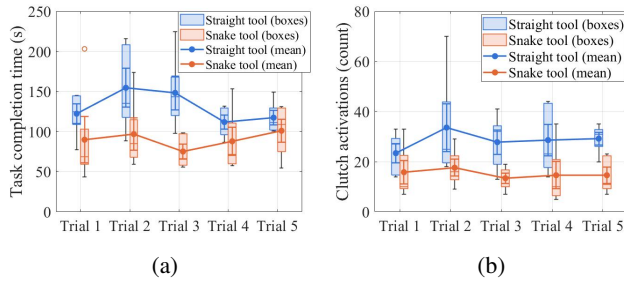
Fig. 8: Comparison of straight tool vs. the snake tool on all users' task completion performance over five trials: (a) completion time, (b) number of clutch activations.
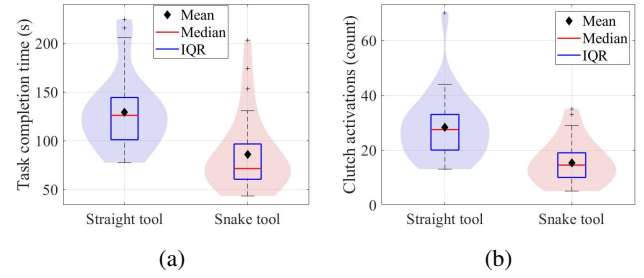

Fig. 9: Comparison of all users' task completion performance while using a straight tool vs. the snake tool, in terms of completion time (a) and number of clutch activations (b).

TABLE II: Comparison of task completion time and number of clutch activations for the straight vs. snake tools, for each and all users ($*$ means $p < 0.05$ and $**$ means $p < 0.01$).

Users	Tool type	Completion time (s)	Clutch (count)
User 1	Straight tool	127.61 ± 46.85	34.83 ± 17.64
	Snake tool	75.82 ± 29.02	16.83 ± 5.67
	p-value	* (0.049)	0.054
User 2	Straight tool	105.19 ± 27.52	28.40 ± 12.09
	Snake tool	86.35 ± 16.63	11.60 ± 5.22
	p-value	0.23	* (0.03)
User 3	Straight tool	127.73 ± 19.20	16.40 ± 3.36
	Snake tool	66.91 ± 16.62	10.0 ± 3.67
	p-value	**	* (0.02)
User 4	Straight tool	114.87 ± 14.63	29.60 ± 8.82
	Snake tool	61.67 ± 14.11	9.0 ± 2.0
	p-value	**	**
User 5	Straight tool	171.20 ± 41.23	31.20 ± 8.25
	Snake tool	140.24 ± 47.09	22.80 ± 8.16
	p-value	0.30	0.14
All users	Straight tool	129.25 ± 37.89	28.34 ± 12.30
	Snake tool	85.96 ± 38.12	15.26 ± 7.73
	p-value	**	**

straight and snake tools. Two measures were analyzed: task-completion time (s) and the count of clutch activations (press events; 0→1 transitions). We interpret both as behavioral indicators of robot/controller intuitiveness and operator comfort, with smaller values reflecting better performance. For each participant, five trials per tool were conducted and the group statistics are reported in Table II. Fig. 8 illustrates, on average, the performance of all users in terms of completion time (Fig. 8a) and the count of clutch activations (Fig. 8b), over five trials. It is observed that the users finished the task faster with fewer clutch activations while using the snake tool. Moreover, their performance was more consistent over

all trials (see the orange curves in Fig. 8), whereas, the mean and distribution of the completion time and clutch counts seem to be relatively inconsistent for the straight tool over different trials (see the blue curves in Fig. 8). For example, the task completion time for all users across all trials is 129.25 ± 37.89 s for the straight tool, which is significantly reduced to 85.96 ± 38.12 s (p <0.01) for the snake tool (see Fig. 9a and Table II). Similar reduction in the clutch activation counts is observed: from 28.34 ± 12.30 for the straight tool to 15.26 ± 7.73 (p <0.01) for the snake tool (see Fig. 9b and Table II). Furthermore, 80% of the users demonstrated, at least in one metric, significantly better performance using the snake tool (Table II).

A NASA-TLX questionnaire is also employed to compare the mental load and user perception of the teleoperative insertion task for the snake and straight tool. Fig. 10 shows the summarized result of the NASA-TLX questionnaire, which includes six criteria: mental demand, physical demand, temporal demand, performance, effort, and frustration. In this questionnaire, lower values indicate lower cognitive load. Their corresponding mean, standard deviation, and p-values are shown in Table III to determine statistical significance. It can be seen that the snake tool reduced the cognitive load for most criteria during the teleoperative insertion task, with four out of six criteria (mental demand, physical demand, performance, and effort) being statistically significant (p <0.05). The large p-value for temporal demand is likely due to the fact that there are no time constraints given to the user to complete the task, as total time taken was used as a metric for performance. Similarly, the large p-value of frustration could indicate the relative difficulty of the task itself, which was kept consistent between the straight and snake tools. Of note, the perceived performance when using the snake tool over the straight tool was most distinct with a mean of 12.8 vs. 4.4 (p-value=0.002) (see Table III). This indicates that the user perceives increased success for the snake tool for teleoperative tasks.

One limitation of this study is the number of users (five). This is a pilot study assessing the feasibility of the integrated robotic systems and the proposed teleoperation control strategy. As future work, we plan to conduct a multi-user follow-up study involving clinicians to perform ERM
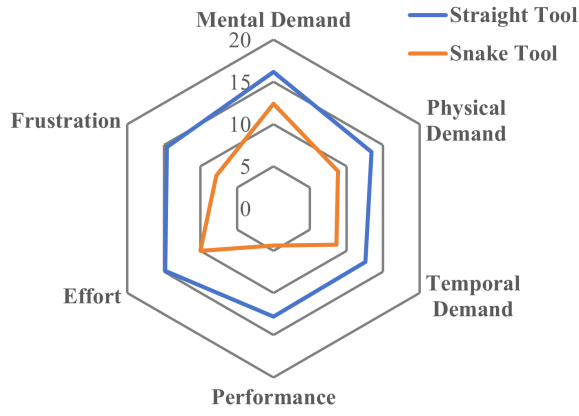
Fig. 10: NASA-TLX questionnaire result.

TABLE III: NASA-TLX questionnaire (mean $\pm$ std, p-value).

Tool Type	Straight	Snake	*p*-value
Mental Demand	16.2 ± 2.3	12.4 ± 1.8	**0.03**
Physical Demand	13.4 ± 5.7	8.8 ± 3.5	**0.01**
Temporal Demand	12.6 ± 5.5	8.6 ± 3.5	0.07
Performance	12.8 ± 1.1	4.4 ± 2.3	**0.002**
Effort	14.8 ± 3.1	10.0 ± 2.3	**0.001**
Frustration	14.6 ± 3.8	7.8 ± 4.0	0.051

peeling using more realistic eye phantoms such as *ex vivo* porcine eyes.

V. CONCLUSIONS

In this work, we developed a high-dexterity vitreoretinal robotic system composed of a 5-DoF base robot (BR) integrated with a 2-DoF snake robot (SR). A combined teleoperation control framework is implemented to provide an intuitive control strategy using the Omega 7 haptic interface. The controller strategy includes an MPC algorithm that enforces the RCM constraint for the BR system and a velocity-based PD controller for the SR system to provide users with the necessary dexterity to achieve optimum approach angle to retina surface. The high-dexterity BR-SR robotic platform was evaluated in both system-level performance experiments and a pilot study with five users. The results of the system-level experiment demonstrated the efficiency and accuracy of the teleoperation control framework in maintaining the RCM constraint for the BR system, as well as providing an optimal approach angle for the hybrid BR-SR robotic system. The results of the pilot user study show that the hybrid BR-SR platform significantly improved the task completion performance compared to the case with the BR-only system. These findings confirm the feasibility and potential of the proposed robotic platform to improve surgical dexterity. Future work will focus on comprehensive kinematic calibration, integration of compensation methods, and validation studies in *ex vivo* porcine eyes.

REFERENCES

[1] R. Channa, I. Iordachita, and J. T. Handa, "Robotic vitreoretinal surgery," *Retina*, vol. 37, no. 7, pp. 1220–1228, 2017.

[2] J. R. Wilkins, C. A. Puliafito, M. R. Hee, J. S. Duker, E. Reichel, J. G. Coker, J. S. Schuman, E. A. Swanson, and J. G. Fujimoto, "Characterization of epiretinal membranes using optical coherence tomography," *Ophthalmology*, vol. 103, no. 12, pp. 2142–2151, 1996.

[3] S. Han, X. Yang, Y. Yang, Y. Zheng, W. Liu, and D. Du, "Numerical simulation of mechanical properties of epiretinal membrane peeling," *Computer Methods in Biomechanics and Biomedical Engineering*, vol. 27, no. 2, pp. 204–210, 2024.

[4] E. Vander Poorten, C. N. Riviere, J. J. Abbott, C. Bergeles, M. A. Nasseri, J. U. Kang, R. Sznitman, K. Faridpooya, and I. Iordachita, "Robotic retinal surgery," in *Handbook of robotic and image-guided surgery*. Elsevier, 2020, pp. 627–672.

[5] S. W. Wong and P. Crowe, "Manipulation ergonomics and robotic surgery—a narrative review," *Annals of Laparoscopic and Endoscopic Surgery*, vol. 9, 2024.

[6] A. Guerroud and P. Vidal, "Smos: stereotaxical microtelemanipulator for ocular surgery," in *Images of the Twenty-First Century. Proceedings of the Annual International Engineering in Medicine and Biology Society,*. IEEE, 1989, pp. 879–880.

[7] T. Meenink, G. Naus, M. de Smet, M. Beelen, and M. Steinbuch, "Robot assistance for micrometer precision in vitreoretinal surgery," *Investigative ophthalmology & visual science*, vol. 54, no. 15, pp. 5808–5808, 2013.

[8] M. A. Nasseri, M. Eder, S. Nair, E. Dean, M. Maier, D. Zapp, C. P. Lohmann, and A. Knoll, "The introduction of a new robot for assistance in ophthalmic surgery," in *2013 35th Annual International Conference of the IEEE Engineering in Medicine and Biology Society (EMBC)*. IEEE, 2013, pp. 5682–5685.

[9] M. Jinno, G. Li, N. Patel, and I. Iordachita, "An integrated high-dexterity cooperative robotic assistant for intraocular micromanipulation," in *2021 IEEE International Conference on Robotics and Automation (ICRA)*. IEEE, 2021, pp. 1198–1204.

[10] M. Esfandiari, P. DuM, H. Wei, P. Gehlbach, A. Munawar, P. Kazanzides, and I. Iordachita, "Model predictive path integral control of i2ris robot using rbf identifier and extended kalman filter*," in *2025 American Control Conference (ACC)*, 2025, pp. 3341–3347.

[11] M. Jinno and I. Iordachita, "Improved integrated robotic intraocular snake," in *2020 International Symposium on Medical Robotics (ISMR)*. IEEE, 2020, pp. 1–7.

[12] A. Alamdar, D. E. Usevitch, J. Wu, R. H. Taylor, P. Gehlbach, and I. Iordachita, "Steady-hand eye robot 3.0: Optimization and benchtop evaluation for subretinal injection," *IEEE transactions on medical robotics and bionics*, vol. 6, no. 1, pp. 135–145, 2023.

[13] A. Deguet, R. Kumar, R. Taylor, and P. Kazanzides, "The cisst libraries for computer assisted intervention systems," in *MICCAI Workshop on Systems and Arch. for Computer Assisted Interventions, Midas Journal*, vol. 71, 2008.

[14] R. Roth, J. Wu, A. Alamdar, R. H. Taylor, P. Gehlbach, and I. Iordachita, "Towards a clinically optimized tilt mechanism for bilateral micromanipulation with steady-hand eye robot," in *2021 International Symposium on Medical Robotics (ISMR)*. IEEE, 2021, pp. 1–7.

[15] B. Xiao, A. Alamdar, K. Song, A. Ebrahimi, P. Gehlbach, R. H. Taylor, and I. Iordachita, "Delta robot kinematic calibration for precise robot-assisted retinal surgery," in *2022 International Symposium on Medical Robotics (ISMR)*. IEEE, 2022, pp. 1–7.

[16] M. Jinno and I. Iordachita, "Improved integrated robotic intraocular snake: Analyses of the kinematics and drive mechanism of the dexterous distal unit," *Journal of medical robotics research*, vol. 6, no. 01n02, p. 2140001, 2021.

[17] E. M. Boctor, R. J. Webster III, H. Mathieu, A. M. Okamura, and G. Fichtinger, "Virtual remote center of motion control for needle placement robots," *Computer Aided Surgery*, vol. 9, no. 5, pp. 175–183, 2004.

[18] C. E. Garcia, D. M. Prett, and M. Morari, "Model predictive control: Theory and practice—a survey," *Automatica*, vol. 25, no. 3, pp. 335–348, 1989.

[19] D. Q. Mayne, J. B. Rawlings, C. V. Rao, and P. O. Scokaert, "Constrained model predictive control: Stability and optimality," *Automatica*, vol. 36, no. 6, pp. 789–814, 2000.